COMPARISON OF DAMAGE CHARACTERISTICS OF ADHESIVELY BONDED AND RIVET-CONNECTED EVTOL WING UNDER BIRD-STRIKE

E. Kayar[1*], G. Abdelal[1], Brian G. Falzon[2] and Z. Kazancı[1]

[1]Advanced Composites Research Group, School of Mechanical and Aerospace Engineering, Queen`s University Belfast, Belfast, United Kingdom

[2] School of Engineering, RMIT University, Melbourne, Australia

Keywords: Bird-strike, EVTOL, Sandwich Structures, Explicit Finite Element Analysis, Smooth Particle Hydrodynamics

ABSTRACT

The advent of electric aircraft, including urban mobility vehicles, has brought renewed attention to the structural integrity of associated lightweight composite airframes. The evolution of composite passenger aircraft demonstrates the advantages of the use of these lightweight materials yet there are still certain structural components which are more susceptible to off-design loading than their metallic counterparts. For example, wing and empennage leading edges, are particularly susceptible to bird strike and are usually still made out of aluminium. Nonetheless, there are certain advantages in pursuing a composite leading edge, such as further weight reduction and enhanced laminar flow. In doing so, it becomes imperative to ensure that its energy absorption characteristics are well understood and can be predicted using computational modelling to reduce the extent of physical testing. For the case of fixed leading edges, energy absorption is likely to be dependent on the way that this leading edge is assembled and attached to the front spar, since the joint itself is a potential energy-absorbing mechanism. In this computational study two approaches are investigated; (i) the leading edge is adhesively-bonded, and (ii) riveted (Fig 1). Soft body impact, to simulate a bird strike, is achieved using Smooth Particle Hydrodynamics (SPH) which is preferred over the Arbitrary Lagrangian Eulerean (ALE) method. The analyses in this study are performed using an explicit finite element solver LS-DYNA. In this article, a composite sandwich wing model, made of unidirectional carbon-fibre polymer composite and a phenolic-based honeycomb core material, is impacted with a soft body mass in accordance with international standards and special conditions given by EASA. These standards are CS-25.631 and the special conditions for eVTOLs. The lay-up of the wing model includes unidirectional prepreg materials pertain to the face and back skin as well as the aforementioned attachment region which connects the spar and the leading edge. The substitute bird model (soft body mass) is configured using a well-defined equation of state model and the properties of homogenous gelatin.

1 INTRODUCTION

The hemispherical capped cylindrical bird model is formed using Smooth Particle Hydrodynamics (SPH). Soft body impact parameters, representative of a physical bird, are correlated with actual bird impact tests from literature.

The maximum cruise speeds of recently developed eVTOLs are shown in Figure *1*. The average cruise speed is approximately 198.5 KPH. The eVTOL design of CityAirbus (NextGen) has the capability to reach 120 KPH while the true air speed of an aircraft is defined as 648.2 KPH for conventional large aircraft at the bird-strike certification requirement of EASA CS 25.631.

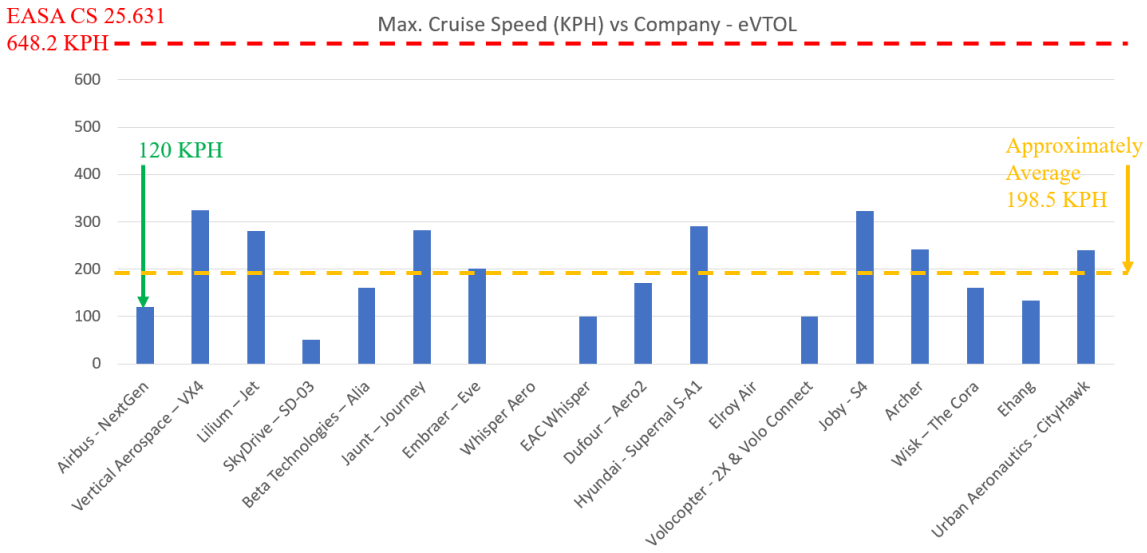

Figure 1: Comparison of the eVTOL cruise speeds

When the flow across a shock is assumed as one dimensional, adiabatic and irreversible, the conservation of mass (continuity) and conservation of momentum equations can be written as in (1) and (2) where u_s and u_p express shock and particle velocity, respectively. Initial pressure and density during shock phase are given using P_1 and ρ_1 where final pressure and density are given using P_2 and ρ_2 respectively in (1) and (2). The Hugoniot pressure is the peak pressure and stagnation pressure is the steady flow pressure occurring after the peak when a homogenous soft body impacts a rigid object, Figure 2 [1].

$$\rho_1 u_s = \rho_2 (u_s - u_p) \tag{1}$$

$$P_1 + \rho_1 u_s^2 = P_2 + \rho_2 (u_s - u_p)^2 \tag{2}$$

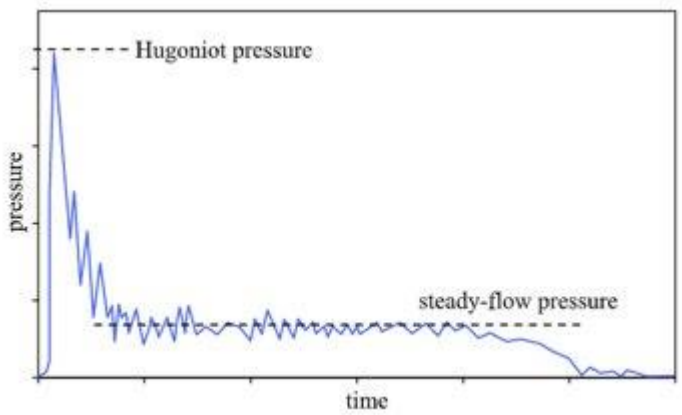

Figure 2: Pressure vs time response of a soft body impact on a rigid plate

In hydrodynamic theory, one-dimensional homogenous soft body impact on a rigid surface has four phases until fully terminated. These phases are shock, release, steady flow and termination respectively [2]. The material at the edge of the bird is subjected to an extremely high pressure gradient as the shock wave propagates through the bird, which accelerates the particles radially outward and creates a release wave. The function of this release wave is to release the radial pressures created by the soft body impact. This pressure results in the emergence of shear stresses greater than

the shear strength of the bird. Finally, a steady flow state is achieved. The four phases are shown in Figure *3* [2].

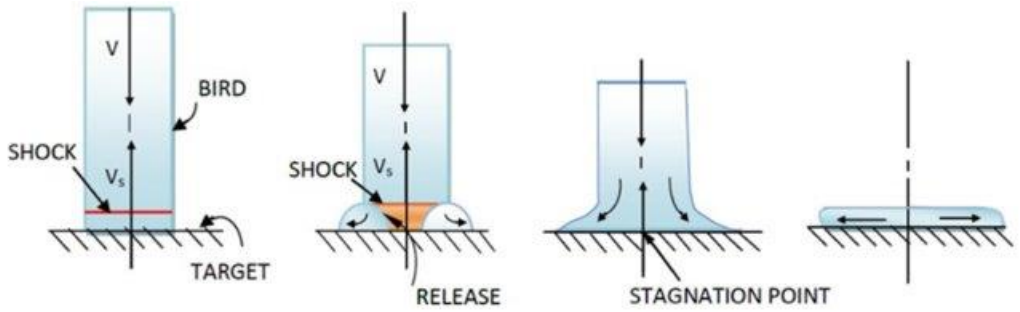

Figure 3: The four phases of a soft body impact on a rigid plate [2]

The principal stress distribution for both rivet-connected and adhesively bonded cases are evaluated to obtain the safety reserve distribution at the critical parts (i.e attachments and spar) under bird-strike. The damage characteristics of both cases are investigated using safety reserve distributions. The workflow of the research target is given in Figure *4*.

Figure 4: Workflow of the research target

In order to fulfil the project's aim of creating a design guideline, this paper compares the damage characteristics of a composite eVTOL wing leading edge, which is adhesively bonded to the rest of the wing structure, with one that is riveted, under bird-strike.

2 THE EXPERIMENTS

Compression and shear experiments using 1/4" x 2" x 2" NOMEX® aramid honeycomb core specimens are carried out in order to obtain force deflection responses including elastic, plateau and densification phases in flatwise and edgewise directions. The experimental setup of flatwise and edgewise compression tests are configured with respect to ASTM C365 (Figure *5*) and ASTM C364 (Figure *8*) standards respectively. Two equivalent stainless steel clamps at both bottom and top sides are used to overcome any instability issues for edgewise compression and shear experiments. The two 2/3" vertical side regions of each cell of the honeycomb specimen are filled using epoxy and the middle 2/3" region of each specimen left free for the shear experiments. No clamps were used for the flatwise compression experiments but the centroid of the setup is aligned with each specimen to avoid any misaligned compression or in-plane bending.

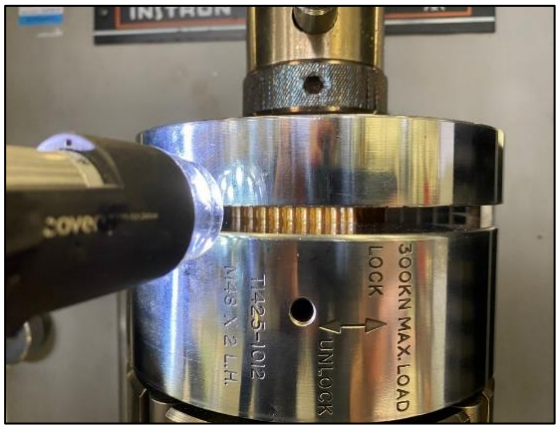

Figure 5: The setup of ASTM C365 (flatwise compression) experiment

The buckling failure mode and the deformed shape of the core after densification phase are shown in Figure 6.

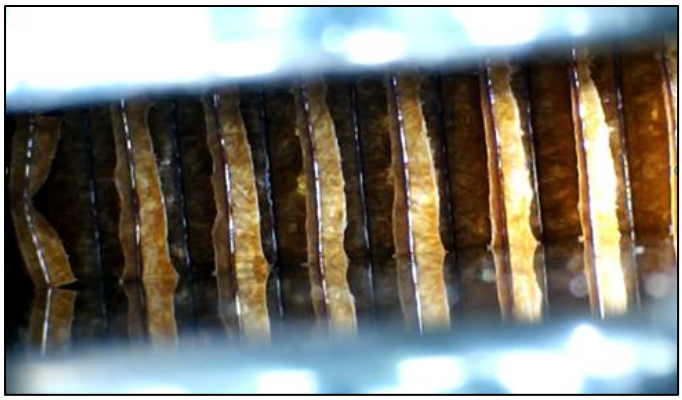

(a) Buckling mode

(b) Deformed shape

Figure 6: Experimental results of flatwise compression of an aramid honeycomb core

The force displacement results of five consecutive experiments show consistently, Figure *7*. The elastic phase is transformed into a plateau phase when the compression load reaches 6 kN. Then, densification starts when 4.5mm of 6.35mm (70.8 % of the thickness) is compressed.

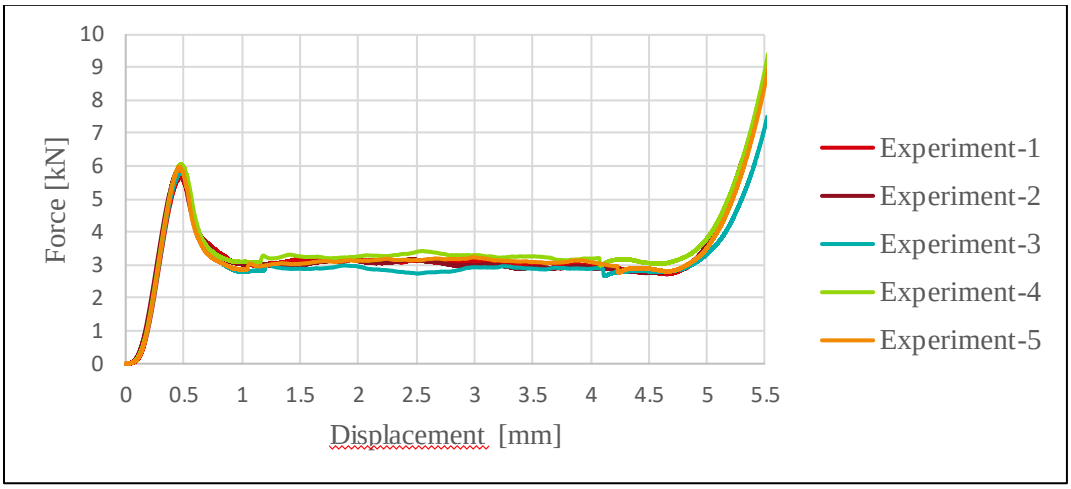

Figure 7: Experimental results of flatwise compression of an aramid honeycomb core - force vs displacement response

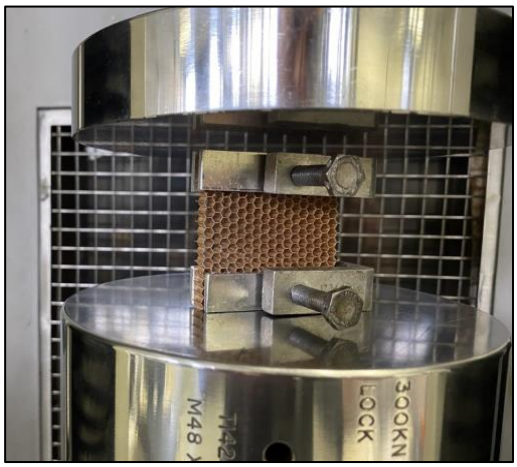

Figure 8: The setup of ASTM C364 (edgewise compression) experiment

The upper and lower rigs of the setup of edgewise compression experiments and the deformed shape after densification phase are shown in Figure *9*.

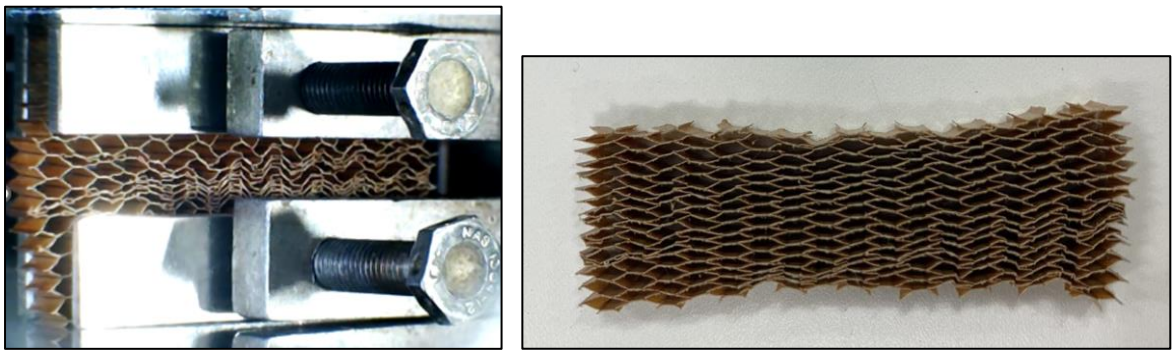

(b) Densification process (b) Deformed shape

Figure 9: Experimental results of edgewise compression of an aramid honeycomb core

The force versus displacement response of the edgewise compression experiments are consistent withth exception of the third and fifth experiments. These two experiments failed because of stability problems. The transformation from elastic region to plateau region is achieved when the load reaches 12 N. Therefore, the elasticity modulus is lower than the flatwise compression case. Additionally, the response curves have different trends. The resultant data is shown in Figure *10* and the local view of the highlighted region in Figure *10* is shown in Figure *11*. The experiments marked using single and double asterisk (experiment-3 and experiment-5) are failed after 15 millimeters and 27 millimetres compression respectively because of instability problems. Therefore, 3rd and 5th experiments are superseded by 6th and 7th experiments.

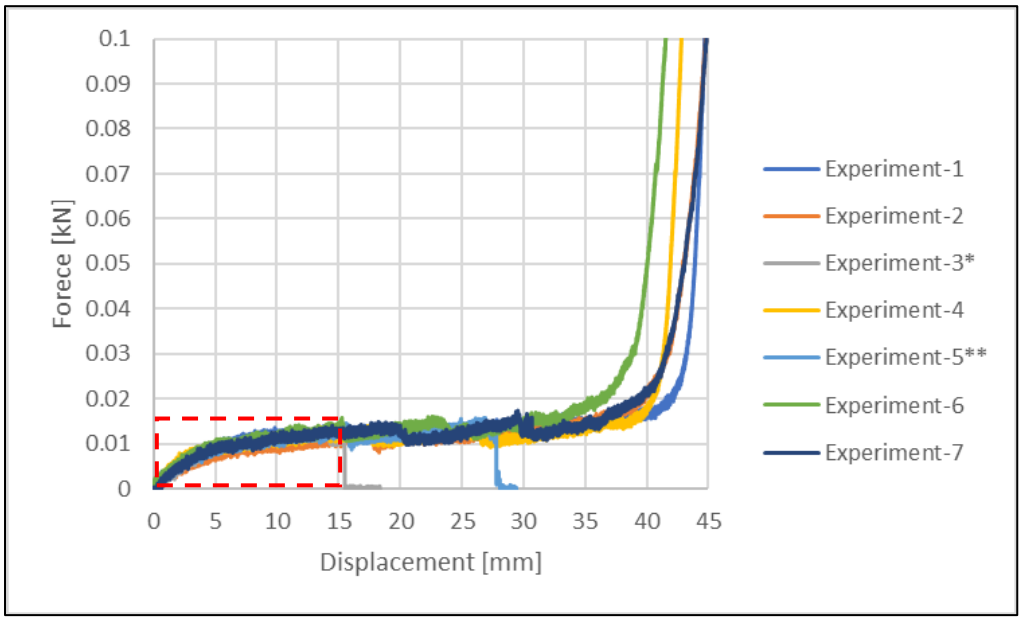

Figure 10: Experimental results of edgewise compression of an aramid honeycomb core - force vs displacement response

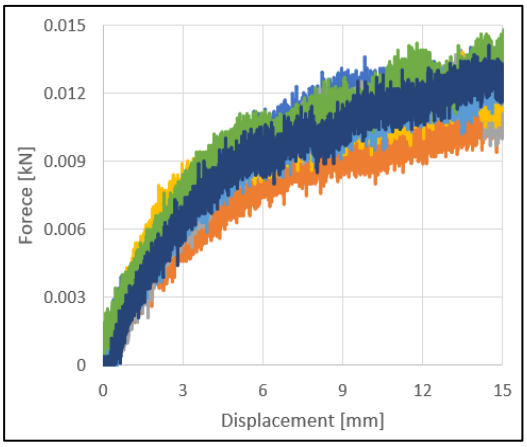

Figure 11: Experimental results of edgewise compression of an aramid honeycomb core - force vs displacement response (0-15 mm)

As well as the compression experiments, shear experiments are performed in order to extract the shear properties of the core. The characterization process includes force versus displacement output

which can be converted into stress versus strain data. The resultant data is implemented in the numerical model to improve the accuracy of the wing model numerical analyses.

The force versus displacement output expresses the nonlinear buckling characteristics of the specimens as well as the absorption characteristics of the core for each direction of loading.

3 NUMERICAL MODEL

The numerical model is configured using shell finite elements for facing and backing skin of the leading edge, spar and attachments, solid finite elements for honeycomb core at leading edge and spar, beam elements for rivets and SPH (Smooth Particle Hydrodynamic) elements for the bird model.

The connection between the unidirectional composite material of the skin and the honeycomb is implemented by tie-break contact assignment instead of cohesive zone modelling.

3.1 Finite Element Model of The Wing Leading Edge of an eVTOL

Two wing finite element model configurations of an eVTOL are configured which have the same material properties, and design variables except the connection details highlighted in Figure 12. The upper and lower attachment parts connect the leading edge to the spar region for the rivet-connected configuration (Figure 12 (a)) and the connector parts which ensure nodal connectivity of the leading edge to the spar in adhesively bonded configuration (Figure 12 (b)).

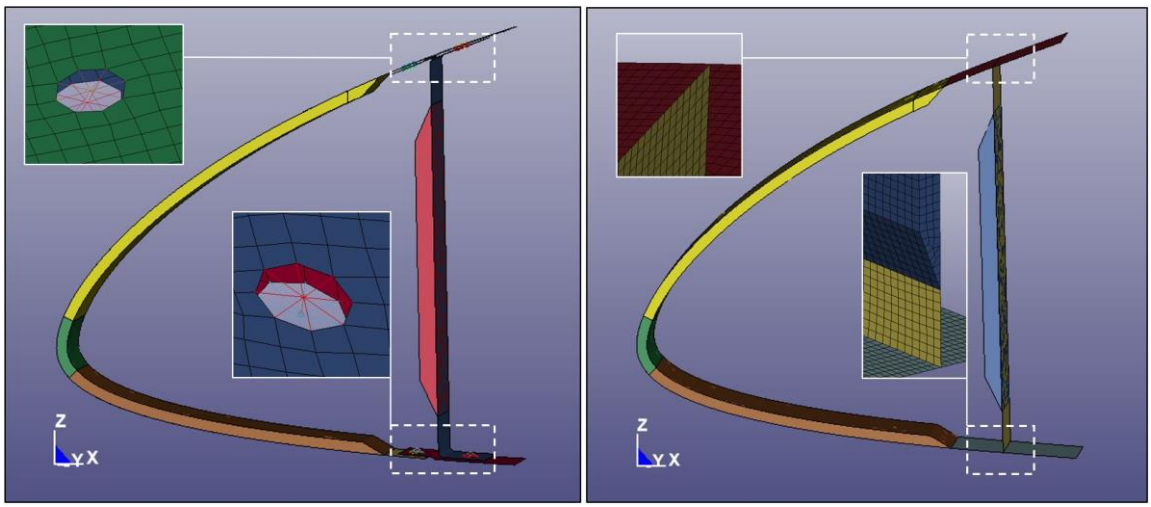

(a) The rivet-connected configuration (b) The bonded configuration

Figure 12: Skin, honeycomb, spar and attachment configurations at the leading edge of the wing.

The riveted configuration has 256 beam elements for the rivets, 175616 shell elements for the facing and backing skin of the leading edge, spar and the attachments, and 18432 solid elements for the honeycomb core. The adhesively bonded configuration has the same number of solid elements but no beam elements, and 182784 shell elements. The average element size of the model is 5 millimeters. The riveted model comprises 452079 nodes and the adhesively bonded model has 444133 nodes including the nodes of the SPH (Smooth Particle Hydrodynamics) bird model. Fully integrated shell element formulation (ELFORM=16) [3] using 3 integration points for each shell element is implemented in addition to (ELFORM=1) [3] for the solid elements which represent honeycomb cores. The rivet connections are configured using *MAT_SPOTWELD (ELFORM=9) [3] represented by cylindrical beams. The diameter of the beams is 4 millimetres and the constant spacing is 40 millimetres. The interaction between the shell and the solid parts are ensured using the tiebreak contact formulation.

3.2 Material Models

The failure index (3) or safety reserve (4) terms are used to evaluate the safety status of each lamina element of a unidirectional or fabric composite lay-up for facing, backing skin, spar and attachments. Tension and compression limits along the fiber and in the transverse direction, and the shear limit are the essential material properties to evaluate these outputs. The material properties of M91/IM7 are assigned to unidirectional composite materials [4]. In addition to the aforementioned properties, numeric interaction term F_{13}, maximum & minimum principal stress and shear stress outputs of the finite element analysis are the required inputs according to Tsai-Wu failure criteria in order to evaluate the safety reserve distribution. The formula of safety reserve is given in (4).

$$\textbf{Failure Index} = \left(\frac{1}{X_t} - \frac{1}{X_c}\right)\boldsymbol{\sigma_1} + \left(\frac{1}{Y_t} - \frac{1}{Y_c}\right)\boldsymbol{\sigma_3} + \frac{\sigma_1^2}{X_t X_c} + \frac{\sigma_3^2}{Y_t Y_c} + \frac{\tau_{13}^2}{S^2} + \boldsymbol{2F_{13}\sigma_1\sigma_3} \tag{3}$$

$$\left[\frac{\sigma_1^2}{X_t X_c} + \frac{\sigma_3^2}{Y_t Y_c} + \boldsymbol{2F_{13}\sigma_1\sigma_3} + \frac{\tau_{13}^2}{S^2}\right]\boldsymbol{SR^2} + \left[\boldsymbol{\sigma_1}\left[\frac{1}{X_t} - \frac{1}{X_c}\right] + \boldsymbol{\sigma_3}\left[\frac{1}{Y_t} - \frac{1}{Y_c}\right]\right]\boldsymbol{SR} = \mathbf{1} \tag{4}$$

X_t: Tension Limit Along Fiber (170 GPa)
X_c: Compression Limit Along Fiber (150 GPa)
Y_t: Tension Limit Transverse Fiber (8.8 GPa)
Y_c: Compression Limit Transverse Fiber (9.4 GPa)
σ_1: 1st Principal Stress - Tension
σ_3: 3rd Principal Stress - Compression
τ_{13}: Shear Stress
S: Shear Limit (5.5. GPa)
F_{13}: Interaction Term (0.5)
SR: Safety Reserve

3.3 Bird Model

A thermodynamic state of a homogenous material, not experiencing any reactions or phase changes can be defined by two state variables. Different forms of the equation of states describe the different types of materials. Pressure and volume are the major parameters for a bird impact scenario. In order to investigate the results of bird impact, substitute bird models made of gelatine are usually used instead of real birds, chickens or gooses in gas gun tests on components with respect to regulations declared by EASA and FAA. This also helps correlation studies because the heterogenous tissue of birds and the bones make the impact side of it important. Hence, bird-like chemical materials (i.e. Porous gelatine) are produced and used. In analyses of bird modelling, the equation of state model is implemented to define the proper pressure versus volume relationship of the homogenous gelatine.

Gruneisen formulation is used to model the homogenous soft body in explicit dynamic numerical analyses. Compressed and expanded equations are given in (5) and (6). The compressed equation and its parameters are used in further simulations in this work. The Gruneisen equation of state with cubic shock-velocity as a function of particle velocity $\boldsymbol{v_s(v_p)}$ defines pressure for compressed materials as in (5). C is the intercept of the $\boldsymbol{v_s(v_p)}$ in velocity units. $\boldsymbol{S_1, S_2}$ and $\boldsymbol{S_3}$ are the dimensionless coefficients of the slope of the $\boldsymbol{v_s(v_p)}$. $\boldsymbol{\gamma_0}$ is the dimensionless Gruneisen gamma, a is the dimensionless first order volume correction to $\boldsymbol{\gamma_0}$ and E denotes the internal energy according to [5].

$$p = \frac{\rho_0 C^2 \mu\left[1 + \left(1 - \frac{\gamma_0}{2}\right)\mu - \frac{\alpha}{2}\mu^2\right]}{\left[1 - (S_1 - 1)\mu - S_2\frac{\mu^2}{\mu+1} - S_3\frac{\mu^3}{(\mu+1)^2}\right]^2} + (\gamma_0 + \alpha\mu)E \tag{5}$$

$$p = \rho_0 C^2 \mu + (\gamma_0 + \alpha\mu)E \qquad \mu = \frac{\rho}{\rho_0} - 1 \tag{6}$$

The diameter of the SPH (Smooth Particle Hydrodynamics) bird model which is used in numerical analyses is calculated using (7) where V_b is volume, W_b is weight and ρ_b is density of the bird model.

$$D = \left(\frac{12V_b}{5\pi}\right)^{1/3} = \left(\frac{12\,W_b}{5\,\pi\,\rho_b}\right) \tag{7}$$

A density of 940 kg/m3 and mass of 1.814 kg were used for the bird in accordance with section 25.631 of the EASA requirements. The resultant dimensions of the substitute bird model used in the simulations are given in Figure *13*. The length of the two hemispherical capped cylindrical bird model is 225mm and the diameter is 110mm. The finite element model of the bird is configured using 15270 SPH elements and the same number of nodes. The nodal distance of the model is 5 millimeters. The interaction between the facing skin of the leading edge and the SPH elements are configured using automatic node to surface contact algorithm. The nodes of the impactor bird model are assigned as slave nodes and the segment set of the facing skin elements are set as master nodes.

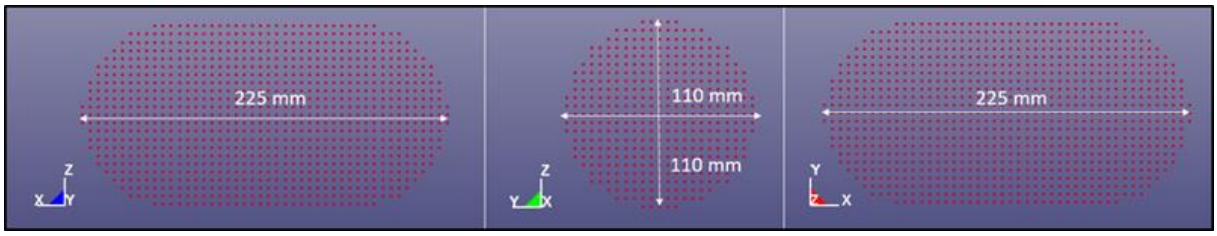

Figure 13: Dimensions of the substitute bird model

4 EXPLICIT FINITE ELEMENT ANALYSES

The simulations are performed by assigning 3.33e4 mm/s initial velocity to the bird in the positive X direction, Figure 14. The magnitude of the velocity decreased to zero at the midside of the bird when the termination time of the simulation was reached, Figure *14*. The far end edges of the upper and the lower attachments are fixed in each translational degree of freedom while the rotational degree of freedoms are kept free to get rid of any stiffening effects. The simulations were solved for 10 ms without using any mass scaling.

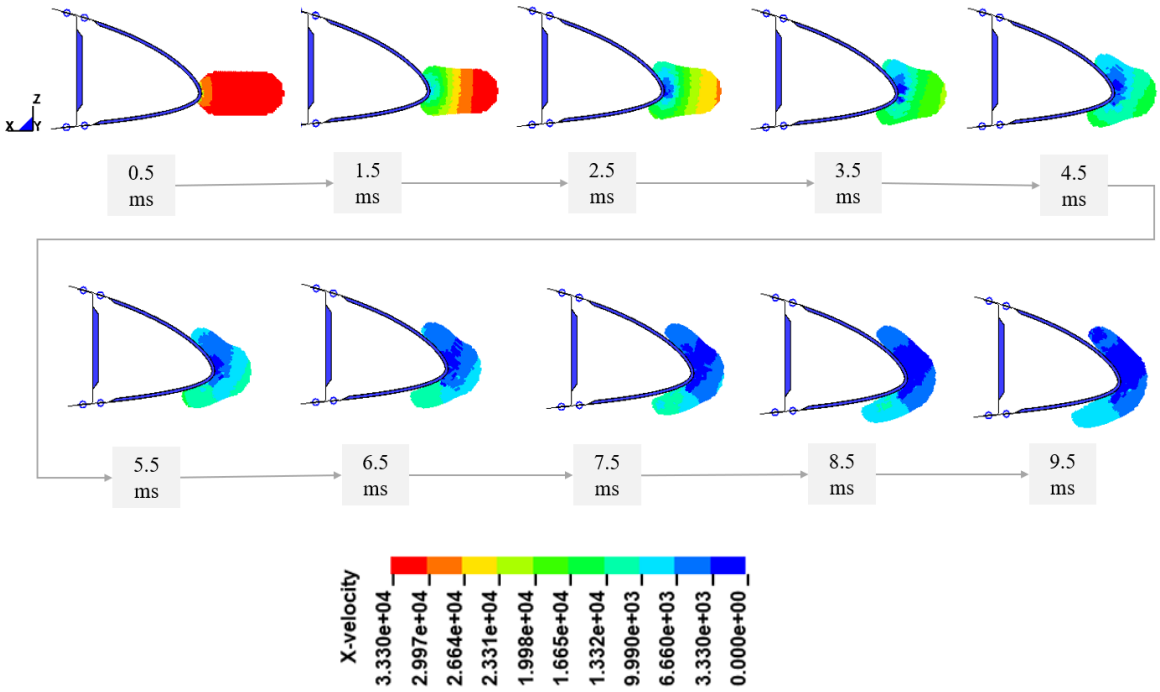

Figure 14: Positive X velocity of the bird

5 RESULTS & DISCUSSION

The maximum (tension) principal stress results are evaluated at the time 2.5 ms as 102.9, 90.2 and 69.7 GPa at upper, lower attachments and spar respectively as shown in Figure *15* and Table *1*. The minimum (compression) principal stress results are also evaluated at the same time to evaluate safety reserve distributions for both rivet connected and adhesively bonded cases.

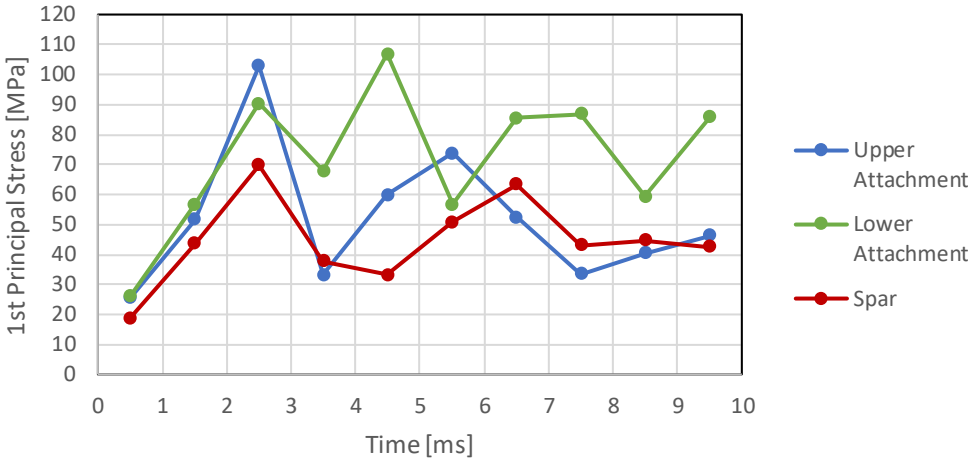

Figure 15: First principal stress results at the attachment parts and spar of the rivet connected case.

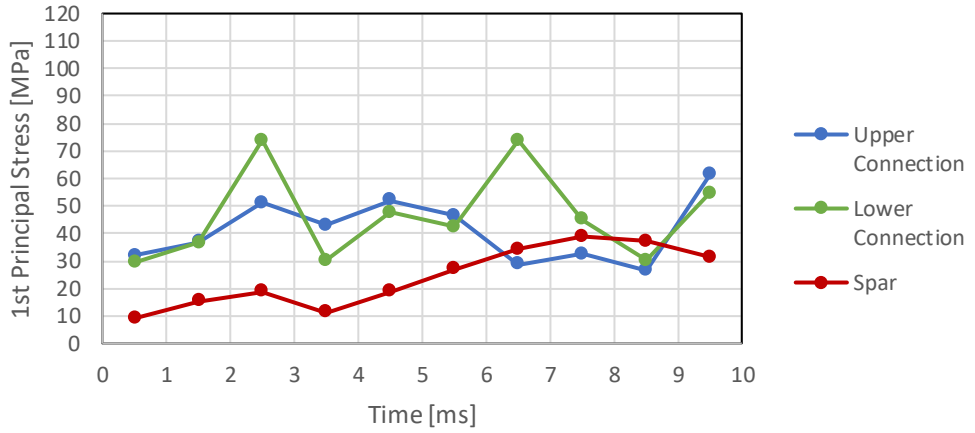

Figure 16: First principal stress results at the connection parts and spar of the adhesively bonded case.

Time [ms]	Upper Attachment & Connection [GPa]		Lower Attachment & Connection [GPa]		Spar, Rivet Connected & Adhesively Bonded [GPa]	
0.5	25.4	31.9	26.0	29.4	18.8	9.1
1.5	51.7	36.8	56.8	36.7	43.7	15.4
2.5	**102.9**	**51.2**	**90.2**	**73.7**	**69.7**	**18.8**
3.5	33.1	42.9	68.0	30.3	37.8	11.1
4.5	60.0	52.0	106.9	47.5	33.3	18.9
5.5	73.8	46.6	56.7	42.3	50.7	27.0
6.5	52.5	28.6	85.6	73.9	63.4	34.1
7.5	33.4	32.5	86.8	45.0	43.0	38.9
8.5	40.3	26.5	59.3	30.3	44.6	37.2
9.5	46.3	61.3	85.8	54.7	42.6	31.2

Table 1: First principal stress results of the attachment & connection parts and spar of the rivet connected and the adhesively bonded cases.

Stress concentration increased at the midside of the rivet connected wing configuration especially at the holes where the rivets connect the attachments to the spar as shown in the Figure 17. Additionally, maximum shear stress (Tresca) are given in Table 2. The maximum & minimum principal stress and maximum shear stress outputs are used in addition to the lamina limits to evaluate the safety reserve. Safety reserve results are given in Table 3.

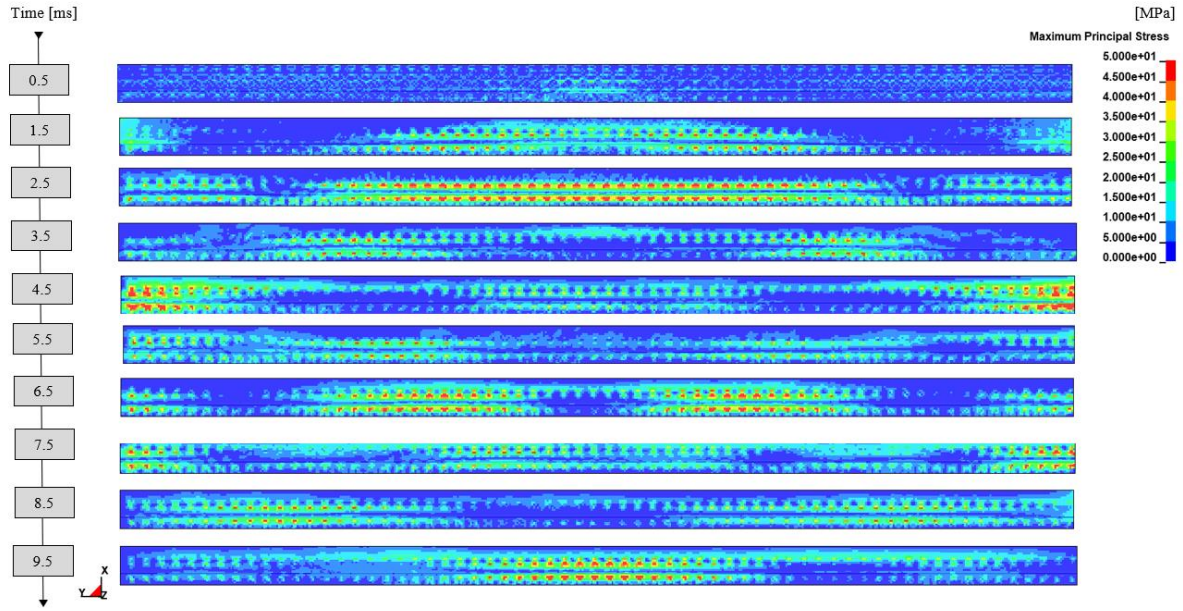

Figure 17: First principal stress distribution at the lower attachment.

Time [ms]	Upper Attachment & Connection)		Lower Attachment & Connection		Spar, Rivet Connected & Adhesively Bonded	
2.5	52.9	29.3	51.3	37.0	36.2	9.4

Table 2: Maximum shear stress (Tresca) results of the attachment & connection parts and spar of the rivet connected and the adhesively bonded cases.

Time [ms]	Upper Attachment & Connection)		Lower Attachment & Connection		Spar, Rivet Connected & Adhesively Bonded	
2.5	9.56e-3	5.3e-3	9.27e-3	6.69e-3	6.54e-3	1.7e-3

Table 3: Safety reserve results of the attachment & connection parts and spar of the rivet connected and the adhesively bonded cases.

6 CONCLUSION

It is essential to ensure a safe design after a series of numerical simulations or tests to pass the bird-strike certification steps for upper & lower attachment parts and the spar of a wing of an aircraft to avoid any unexpected damage which may cause improper landing, take off or fatalities. The safety reserve results at these three critical parts of both rivet connected and adhesively bonded configurations of the wing model are evaluated using the maximum, minimum principal stress, maximum shear (Tresca) stress outputs and the tension & compression limits of M91 unidirectional material along and transverse fiber directions using the Tsai-Wu equation (Eq. (4)) and given in Table 3. Theoretically, safety reserve below 1.0 means the composite structure fails under the assigned loading condition. Therefore, damage is initiated at these parts of the composite wing structure under applied bird-strike loading condition for both configurations but the safety reserve results of the rivet connected configuration are higher than the adhesively bonded configuration and close to the safe region at any connection part and the spar according to Table 3. In conclusion, the composite lay-up of the wing particularly at the attachment and connection parts and the spar are going to be enhanced using a well-developed design which can result in greater safety reserve outputs to make a comprehensive decision about comparing both rivet connected and adhesively bonded configurations properly by using various design variables.

ACKNOWLEDGEMENTS

This research has been kindly funded by a special research scholarship of Queens University Belfast (Project code: R5252MEE). The engineers, technicians and workers of the test laboratories at The Northern Ireland Composites and Engineering Centre (NIACE) supported the material test campaigns.

REFERENCES

[1] S. Heimbs, Computational methods for bird strike simulations: A review, *Computers and Structures*, **89**, 2011, pp. 2093-2112.

[2] M. Guida, F. Marulo, F. Z. Belkhelfa, and P. Russo, A review of the bird impact process and validation of the SPH impact model for aircraft structures, *Progress in Aerospace Sciences*, **129**, 2022.

[3] *LS-DYNA® Keyword User`s Manual Volume 1 Material Models*, United States, 2021.

[4] R. Bogenfeld, J. Kreikemeier and T. Wille, Review and benchmark study on the analysis of low-velocity impact on composite laminates, *Engineering Failure Analysis*, **86**, 2018, pp. 72-99.

[5] *LS-DYNA® Keyword User`s Manual Volume 2 Material Models*, United States, 2021.

[6] R. Hedayati and S. Ziaei-Rad, A new bird model and the effect of bird geometry in impacts from various orientations, *Aerospace Science and Technology*, **28**, 2013, pp. 9-20.

[7] V. K. Goyal, C. A. Huertas, J. R. Borrero, and T. R. Leutwiler, Robust bird-strike modeling based on ALE formulation using LS-DYNA, *Structural Dynamics and Materials Conference*, Vol. 3, 2006, pp. 2044-2061.

[8] M. A. Lavoie, A. Gakwaya, and M. Nejad Ensan, Application of the SPH Method for Simulation of Aerospace Structures under Impact Loading, *10th International LS-DYNA Users Conference*, Detroit, 2008.

[9] A. Haufe, S. Cavariani, C. Liebold, T. Usta, T. Kotzakolios, E. Giannaros, V. Kostopoulos, A. Hornig, M. Gude, N. Djordjevic, R. Vignjevic and M. Meo, On Composite Model Calibration for Extreme Impact Loading Exemplified on Aerospace Structures, *16th International LS-DYNA Users Conference*, Detroit, 2020.

[10] C. Tho, and M. R. Smith, Accurate bird strike simulation methodology for BA609 tiltrotor, *Journal of the American Helicopter Society*, **56**, 2011.

[11] F. Allaeys, G. Luyckx, W. van Paepegem and J. Degrieck, Characterization of real and substitute birds through experimental and numerical analysis of momentum, average impact force and residual energy in bird strike on three rigid targets: A flat plate, a wedge and a splitter, *International Journal of Impact Engineering*, **99**, 2017, pp. 1-13.

[12] T.Bru, *Material characterization for crash modelling of composites*, Gothenburg, 2018.

[13] *Standard Test Method for Edgewise Compressive Strength of Sandwich Constructions ASTM C364/C364M-07,* ASTM International, United States, 2012.

[14] *Standard Test Method for Flatwise Compressive Properties of Sandwich Cores C365/C365 M – 22,* ASTM International, United States, 2022.

[15] I. C. Metz, J. Ellerbroek, T. Mühlhausen, D. Kügler, and J. M. Hoekstra, The bird strike challenge, *MDPI Aerospace*, **7**, 2020.

[16] F. Plassard and H. Abdulhamid, Test and simulation approach toward the certification of an aircraft structure subjected to a bird strike, 2017.